Nanoscale

PAPER

View Article Online
View Journal | View Issue

Cite this: *Nanoscale*, 2018, **10**, 1517

Biodegradable MoO_x nanoparticles with efficient near-infrared photothermal and photodynamic synergetic cancer therapy at the second biological window†

Wenyan Yin, [a] Tao Bao,[a] Xiao Zhang,[a] Qin Gao,[a] Jie Yu, [a] Xinghua Dong,[a] Liang Yan, [a] Zhanjun Gu *[a] and Yuliang Zhao[a,b]

Received 25th October 2017,
Accepted 1st December 2017

DOI: 10.1039/c7nr07927c

rsc.li/nanoscale

Near-infrared (NIR) laser induced phototherapy has been considered as a noninvasive option for cancer therapy. Herein, we report plasmonic PEGylated molybdenum oxide nanoparticles (PEG-MoO_x NPs) that were synthesized by using a facile hydrothermal method. The PEG-MoO_x NPs exhibit broad absorption at the NIR biological window and remarkable photothermal conversion ability in the first (808 nm) and the second (1064 nm) windows. Moreover, the biocompatible PEG-MoO_x NPs exhibit effective cellular uptake and could be eliminated gradually from the liver and spleen in mice. Studies on the therapeutic effects of these NPs under 808 and 1064 nm exposures with mild hyperthermia are conducted. According to the result, exposure to 1064 nm irradiation can not only effectively convert light into heat but also sensitize the formation of reactive oxygen species (ROS), which exert dramatic cancer cell death and suppression *in vivo* due to the synergic effect of photothermal therapy (PTT) and photodynamic therapy (PDT). In marked contrast, 808 nm irradiation can only execute limited PTT to cancer cells, showing a relatively low inhibition rate *in vitro* and *in vivo*. This biodegradable MoO_x nanoplatform with synergetic PTT and PDT functionalities upon 1064 nm irradiation provided emerging opportunities for the phototherapy of cancer in nanomedicine.

1. Introduction

Cancer is one of the most life-threatening diseases.[1] Several therapeutic approaches such as chemotherapy, radiotherapy, operative treatment, and so on have been developed for cancer treatment. Among these approaches, near-infrared (NIR) laser induced photothermal therapy (PTT) and photodynamic therapy (PDT) are two major phototherapeutic approaches for cancer treatment.[2] PTT can ablate cancer cells by transforming light into heat energy, while PDT mainly induces cell apoptosis due to the reactive oxygen species (ROS) generated by photosensitizers.[3,4] Both these approaches possess unique advantages including remote controllability, minimal invasiveness to normal tissues as well as low systemic toxicity. In addition, biological tissues have a minimal NIR light absorbance in the first (650–950 nm, NIR-I) window and the second (1000–1350 nm, NIR-II) window.[5,6] Water is the most significant component and the major absorber of NIR light in biological tissue. The lower water absorption of 808 nm and 1064 nm laser irradiation in the NIR-I/NIR-II window not only results in a deeper penetration depth, but also minimizes tissue overheating.[7] In particular, the NIR-II laser has deeper penetration depth and maximum permissible exposure to skin when compared to the NIR-I laser.[8] The penetration depth is deemed to be maximal for 1000–1100 nm light, and the maximum permissible exposure for skin is 1.0 W cm^{-2} in this spectral region.[9] With the rapid development of nanotechnology, numerous PTT nanoagents with an intrinsic NIR photothermal conversion effect in the NIR-I and NIR-II windows were reported.[10–15] Meanwhile, it has been reported that metal nanomaterials (Au and Pt) can act as NIR light activatable nanoagents without additional organic photosensitizers in the NIR-I window for the PDT of cancer due to their ability to form singlet oxygen ($^1O_2$).[16–18] Recently, Vankayala *et al.* reported Au nanorods as a nanoagent for synergetic PTT and PDT under the NIR-II window irradiation for the complete destruction of solid tumors.[19] However, a Au nanoagent often requires the use of expensive femto-second lasers to achieve PTT and PDT efficacy. In particular, NIR-II light activatable nanoagents,

[a]*Key Laboratory for Biomedical Effects of Nanomaterials and Nanosafety, Institute of High Energy Physics, Chinese Academy of Sciences, Beijing 100049, China. E-mail: zjgu@ihep.ac.cn*

[b]*National Center for Nanosciences and Technology of China, Beijing 100190, China*

†Electronic supplementary information (ESI) available. See DOI: 10.1039/c7nr07927c

which have the function of synergetic PTT and PDT for cancer therapy, are very rare. Besides this, most of the nanoagents with synergetic PTT and PDT function were always obtained by introducing organic photosensitizers to the surface of photoagents, and the process is complicated, which may cause unwanted fluorescence quenching of the photosensitizer.[20] Organic photosensitizers also possess low molar extinction coefficients, and can undergo photobleaching. Therefore, it is highly desired to develop a novel NIR-II activatable nanoagent with a simple synthesis process, while it possesses both high photothermal conversion efficiency and direct ROS production ability in the NIR-II window to effectively treat tumors by synergetic PTT and PDT.

Transition metal oxide semiconductor nanomaterials are of particular interest due to their tunable localized surface plasmon resonance (LSPR).[21–24] Considerable efforts have been undertaken using plasmonic semiconductor nanomaterials ($Cu_{2-x}S$, $W_{18}O_{49}$) for synergetic PTT and PDT, which were mainly focused on the NIR-I window irradiation.[25–28] Until now, the investigation of NIR-II based phototherapy using semiconductor nanomaterials is still rare. As an emerging type of NIR plasmonic semiconductor, oxygen-deficient molybdenum oxide nanoparticles (MoO_x NPs) are easy to be synthesized at a low cost in comparison with noble metal nanomaterials. For instance, it was demonstrated that the band gap of sub-stoichiometric MoO_x is shape-dependent.[29] Blue-shifting and red-shifting phenomena have been observed in nanoparticles and nanoflakes, respectively.[29] Moreover, the LSPR of MoO_x can be tuned in the NIR region through changing its chemical composition, which allows the modulation of its optical properties.[30,31] Our group recently reported that hollow structured MoO_x NPs possess strong NIR-I (808 nm) absorption and good NIR-I triggered photothermal/chemotherapy synergistic effects on tumors.[32] All these findings have indicated that MoO_x NPs are a promising candidate as meritorious NIR phototherapeutic nanoagents.[33] In addition, the long-term toxicity of nanomaterials could be a serious concern which hampers their further clinical application.[31] Therefore, it would be better to develop a kind of MoO_x NP which can be excreted from normal tissues to avoid the potential long-term toxicity of the NPs while being accumulated in tumors efficiently *via* the enhanced permeability and retention (EPR) effect. However, PEG-MoO_x NPs as a biodegradable, single-phase, dual-functional nanoagent that presents a combined PTT and PDT effect in the NIR-II window have not been reported to date.

Herein, we develop PEGylated MoO_x nanoparticles (PEG-MoO_x NPs) with a diameter of 15–25 nm that were synthesized through a facile, green, one-pot hydrothermal method. The low cost, plasmonic PEG-MoO_x NPs present remarkable NIR absorption in the range from 800 to 1200 nm. Meanwhile, the PEG-MoO_x NPs containing essential trace elements of the human body (O and Mo) exhibit good biocompatibility. The biocompatible PEG-MoO_x NPs exhibit considerable photothermal conversion efficiency, effective cellular uptake and a gradual elimination from the liver and spleen of mice. The PEG-MoO_x NPs as a photo-responsive agent for the destruction of cancer cells in the NIR-I (808 nm) and NIR-II (1064 nm) windows under mild hyperthermia (~43 °C), which can avoid high temperature induced damage to normal tissues, were investigated. We firstly found that the 1064 nm irradiation can not only effectively convert laser irradiation into heat but also sensitize PEG-MoO_x NPs to generate $^1O_2$, achieving effective suppression of tumors in mice due to the synergistic PTT and PDT effect. Consequently, the PEG-MoO_x NPs as a simple but promising nanoplatform provided an emerging opportunity for the phototherapy of cancer in the field of nanomedicine.

2. Experimental section

2.1 Materials and reagents

Ammonium molybdate tetrahydrate [$(NH_4)_6Mo_7O_{24}{\cdot}4H_2O$] and polyethylene glycol (PEG, M_w = 4000) were purchased from Aladdin Co. Ltd. Ethanol was purchased from Beijing Chemical Corporation. All the chemicals were of research grade and used without further purification. Distilled water was used throughout.

2.2 Synthesis of PEG-MoO_x NPs

Firstly, 0.07 mmol of $(NH_4)_6Mo_7O_{24}{\cdot}4H_2O$ was dissolved into 20 mL of distilled water under stirring. Afterwards, 10 mL of PEG-4000 (0.10 g) was added into an ethanol solution (volume ratio of water to ethanol = 2 : 1). The pH of the solution was adjusted to 1.2 by using hydrochloric acid (HCl). After mixing evenly, the hydrothermal process was performed at 160 °C for 12 h and a blue precipitate was observed. The precipitate was collected by centrifugation and washed with distilled water three times. Finally, the products were obtained by freeze-drying.

2.3 Photothermal effect of PEG-MoO_x NP aqueous solution

To determine the photothermal effect, we measured the temperature increment (ΔT) when the continuous laser of 808 nm and 1064 nm laser wavelengths respectively irradiated the PEG-MoO_x NPs. PEG-MoO_x NP aqueous solutions with different concentrations were put into a quartz cuvette and irradiated (808 nm and 1064 nm laser) at a power density of 1.0 W cm^{-2} for 10 min. To test the photostability of the PEG-MoO_x NPs (reproducibility of the heating process) *via* 808 nm and 1064 nm laser irradiation, five cycles of NIR laser irradiation were performed for the PEG-MoO_x NPs solution with concentrations of 1.0 mg mL^{-1}. Each cycle consisted of 3 min irradiation followed by a 3 min cooling phase.

2.4 *In vitro* cell viability assay of PEG-MoO_x NPs

HeLa cells (a human cervical carcinoma cell line), HepG2 cells (a human liver hepatocellular cell line), and PANC-1 cells (a human pancreatic cancer cell line) were purchased from Cancer Hospital, Chinese Academy of Medical Sciences. Then,

the HeLa cells, HepG2 cells, and PANC-1 cells were cultured with Dulbecco's modified Eagle's medium (DMEM), Iscove's modified Dulbecco's medium (IMDM), and RPMI 1640 medium, respectively, which were supplemented with 10% fetal bovine serum (FBS), at 37 °C under a humidified atmosphere with 5% CO_2. The cell viabilities were evaluated using the standard Cell Counting Kit-8 (CCK-8) assay. The three types of cells were seeded into 96-well culture plates (about 8×10^3 cells per well). After adding PEG-MoO_x NPs with different concentrations (3.125, 6.25, 12.5, 25, 50, 100, and 200 μg mL^{-1}), these cells were subsequently incubated for 24 h at 37 °C under 5% CO_2. Then, 10% of the CCK-8 medium solutions was added to each well and incubated for another 2 h. Finally, the absorbance was measured at 490 nm using SpectraMax M2 (MDC, USA). Six replicates were taken for each treatment group.

2.5 Extracellular ROS detection

1,3-Diphenylisobenzofuran (DPBF) was used as a singlet $^1O_2$ trapping reagent in acetonitrile solution. The generation of extracellular ROS was measured with the DPBF probe. In a typical experiment, 3 mL of acetonitrile solution containing 0.08 mM DPBF and 100 μg mL^{-1} PEG-MoO_x NPs were placed in a quartz cuvette. 808 nm and 1064 nm lasers (power density for 808 nm: 1.2 W cm^{-2}, power density for 1064 nm: 1.0 W cm^{-2}) were used as the laser source. The absorbance of the solution at 410 nm was measured for a 30 min period using a UV-vis spectrophotometer. The decrease of the absorbance caused by the photobleaching of DPBF was measured and corrected in all the experiments.

2.6 Measurement of intracellular ROS production

A typical ROS-sensitive probe, dichlorofluorescein diacetate (DCFH-DA) solution, which could be oxidized into highly fluorescent DCF by ROS, was chosen to detect the intracellular ROS generation. Firstly, HeLa cells with a density of 1×10^5 cells per well were plated in 6-well plates for 12 h. The cells were incubated with PEG-MoO_x NPs (100 μg mL^{-1}) for 2 h and irradiated with 808 nm (power density: 1.2 W cm^{-2}, with the maximum temperature control at 43 °C) or 1064 nm laser (power density: 1.0 W cm^{-2}, with the maximum temperature control at 43 °C) for 10 min. The cell medium was then replaced with DCFH-DA solution, followed by co-incubation for 30 min at 37 °C in the dark. The group treated with the standard ROS inducing reagent ROSup (100 μM) without PEG-MoO_x NPs was defined as the positive control, while the group without any treatment was defined as the negative control. In addition, the group with PEG-MoO_x NPs and 250 μM ROS quenchers (histidine and mannitol), under 1064 nm irradiation, was also used as the control group. Fluorescence microscopy images were obtained with an inverted fluorescence microscope (OLYMPUS X-73, Japan) to evaluate the visualized ROS generation. For DCF detection, the excitation wavelength was 485 nm and the emission wavelength was 525 nm.

2.7 Quantification of the cellular uptake of PEG-MoO_x NPs

To quantify the cellular uptake of PEG-MoO_x NPs, HeLa cells were seeded into 6-well plates with complete DMEM at a density of 2×10^5 cells per well for 24 h; then the medium was removed and replaced with DMEM containing 6.25, 25, and 100 μg mL^{-1} PEG-MoO_x NPs. Meanwhile, the cells were incubated with the PEG-MoO_x NPs at different time interval of 2, 6, and 24 h with four wells at each time point. The HeLa cells were lightly washed three times with PBS, digested with 0.25% trypsin containing 0.02% EDTA, centrifuged for 15 min at 1200 rpm, and collected. Then, an inductively coupled plasma mass spectrometry (ICP-MS) experiment was conducted to quantify the cellular uptake of the PEG-MoO_x NPs. Typically, the above samples were added into 5 mL of HNO_3, transferred to flasks, and sealed for pre-digestion overnight. The next day, 3 mL of 30% H_2O_2 was added to each flask. The flasks were placed on a hot plate and maintained at 150 °C for 3 h until the digestion was complete and then cooled to room temperature. The solution in each flask was diluted to 3 g with 2% HNO_3. A series of Mo standard solutions (0, 0.5, 1, 5, 10, 50, and 100 ppb) were prepared with 2% HNO_3 solution. Both the standard and test solutions were measured by using an ICP-MS system (Thermal Elemental X7, Thermal Fisher Scientific Inc., USA). The amount of PEG-MoO_x NPs was finally normalized to the cell number per gram.

2.8 Combined PTT and PDT efficiency at the cellular level

HeLa, HepG2, and PANC-1 cells were cultured in a 96-well culture plate at a density of 1×10^4 cells per well for 12 h to allow cell attachment. Solutions containing PEG-MoO_x NPs with different concentrations were added to the culture medium. After 4 h of co-incubation, the three types of cells were irradiated with 808 nm (1.2 W cm^{-2}) and 1064 nm lasers (1.0 W cm^{-2}) for 10 min at the surrounding temperatures of 37 °C and 4 °C. Then, these cells were incubated for another 24 h and the cell viabilities were evaluated *via* the CCK-8 assay.

Furthermore, HeLa cells were chosen for investigating cell viabilities by using live/dead staining based on calcein AM/propidium iodide (CA/PI). The HeLa cells were seeded in culture dishes (about 1×10^5 cells per well) overnight at 37 °C under 5% CO_2. Then, the cells were incubated with 50 and 100 μg mL^{-1} concentrations of PEG-MoO_x NPs. After 24 h, the HeLa cells were washed with PBS. The cells incubated with 100 μg mL^{-1} of PEG-MoO_x NPs were irradiated with 808 nm (1.2 W cm^{-2}) and 1064 nm (1.0 W cm^{-2}) lasers for 10 min. After 2 h, the cells were slightly washed with PBS and stained with CA/PI for 15 min. The images were visualized with an inverted fluorescence microscope (OLYMPUS X-73, Japan).

For flow cytometry (FACS), HeLa cells were seeded in 6-well culture plates and divided into six groups: (I) Control, (II) Control + 808 nm, (III) Control + 1064 nm, (IV) PEG-MoO_x NPs (100 μg mL^{-1}), (V) PEG-MoO_x NPs + 808 nm, and (VI) PEG-MoO_x NPs + 1064 nm. After NIR laser irradiation (power density of 808 nm: 1.2 W cm^{-2}, power density of 1064 nm: 1.0 W cm^{-2}) for 10 min, the HeLa cells were incubated for a

further 4 h at 37 °C in the dark. Cells incubated with PBS with or without NIR irradiation served as the control groups. A cell suspension was prepared consecutively by trypsinization, and washing with cold PBS. Then, the cells were stained by using an annexin V-FITC and PI staining kit. The induction of apoptosis in HeLa cells was examined with a FACS Calibur flow cytometer (BD, Accuri C6).

2.9 *In vitro* hemolysis assay

To further evaluate the *in vitro* biocompatibility, ethylenediamine tetraacetic acid (EDTA)-stabilized blood samples were obtained from Kunming mice. All the animal experiments were performed in compliance with the guidelines for the use and care of laboratory animals of the Ministry of Science and Technology of the People's Republic of China. The Animal Study Committee of the Ministry of Science and Technology of the People's Republic of China has approved the experiments. First, 1 mL of blood sample was added to 2 mL of PBS, and then red blood cells (RBCs) were separated from serum by centrifugation at 2000 rpm for 10 min, washed several times with PBS, and then diluted into 10 mL using PBS. Then, 0.2 mL of diluted RBC suspension was taken out to mix with (I) 0.8 mL of PBS as a negative control, (II) 0.8 mL of deionized water as a positive control, and (III) 0.8 mL of PEG-MoO_x NP dispersions with concentrations ranging from 0 to 800 μg mL^{-1}. Afterward, all the mixtures were vortexed and kept at room temperature for 4 h and centrifuged at 12 000 rpm for 5 min. The absorbance of the supernatants at 541 nm was measured by UV-vis spectroscopy. The hemolysis percentage of RBCs was calculated using the following equation: Hemolysis percentage (%) = $(A_{sample} - A_{negative})/(A_{positive} - A_{negative}) \times 100\%$, where A_{sample}, $A_{negative}$, and $A_{positive}$ are the absorbance of the sample, the negative control, and the positive control, respectively.

2.10 *In vivo* toxicity assessment of PEG-MoO_x NPs

BALB/c mice (male, 5 weeks old) were randomly divided into different groups (n = 3 for each group). The PEG-MoO_x NPs (20 mg kg^{-1}, 2 mg mL^{-1}, 200 μL) in PBS were intravenously (i.v.) injected into the tail vein of the mice. The mice injected with PBS (200 μL) acted as the control group. To examine the *in vivo* toxicity, the body weights within 30 days were monitored after injection. The main organs including the heart, liver, spleen, lung, and kidney were removed after the treatment of different days and were fixed in formalin solutions. Then, the organs were dehydrated using buffered formalin, ethanol, and xylene. Finally, they were embedded in liquid paraffin, sectioned, and stained with hematoxylin and eosin (H&E) for histological examination. The pathology slices were observed and photos were taken using an inverted fluorescence microscope. In addition, on the 15th and 30th day, blood chemistry analysis of mice after administration with PEG-MoO_x NPs was carried out. The main indicators for the liver and kidney were investigated *via* routine clinical methods and compared with the control group injected with PBS.

2.11 *In vivo* biodistribution and biocompatibility of PEG-MoO_x NPs

Healthy male BALB/c mice were i.v. treated with PEG-MoO_x NPs (20 mg kg^{-1}) by tail vein injection. The mice (n = 3 for each group) were then euthanized at different time points (1 h, 12 h, 2 days, 7 days, 15 days, and 30 days). The mice injected with PBS acted as the control group. Major organs including the heart, liver, spleen, lung, and kidney were collected and weighed. Then, all the tissues were treated with HNO_3 and H_2O_2 (v/v = 1 : 1) at 100 °C to obtain clear solutions. The Mo concentrations in the solutions were determined by ICP-MS and the content in each tissue was calculated.

2.12 Tumor animal model and *in vivo* infrared thermal imaging

BALB/c nude mice (male, 5–6 weeks old) were purchased from Cancer Institute & Hospital, Chinese Academy of Medical Sciences. For the pancreatic tumor (PANC-1) model, the nude mice were inoculated subcutaneously with PANC-1 cells (2×10^6) in the right axilla. The tumor size was measured periodically using a slide caliper. When tumor volumes approached ~240 mm^3, the mice were used. For infrared thermal imaging, the tumor-bearing nude mice were anaesthetized using pentobarbital (1%) at a dosage of 100 μL and then injected with PBS (200 μL) and PEG-MoO_x NPs (200 μL, 20 mg kg^{-1}) *via* i.v. injection. Afterwards, the mice were imaged under 808 nm and 1064 nm laser irradiation for 10 min.

2.13 *In vivo* antitumor activity of PEG-MoO_x NPs

The tumor-bearing BALB/c nude mice were also prepared by inoculating 2×10^6 PANC-1 cells through subcutaneous injection. After the tumor volumes reached 240 mm^3, the mice were randomized into six groups (n = 3 for each group): Group I: PBS, Group II: PBS + 808 nm laser, Group III: PBS + 1064 nm laser, Group IV: PEG-MoO_x NPs, Group V: PEG-MoO_x NPs + 808 nm laser, Group VI: PEG-MoO_x NPs + 1064 nm laser. All the tumor-bearing mice were anaesthetized and treated with i.v. injection. The injected dosage was chosen as follows: PBS (200 μL) and PEG-MoO_x NPs (200 μL). For the NIR laser irradiation groups, the tumor sites were irradiated with 808 nm (0.75 W cm^{-2}) and 1064 nm (0.6 W cm^{-2}) lasers for 10 min. The temperature of the irradiated tumor area was recorded. The tumor sizes and the body weights were monitored every two days. On the 15th day, the mice were euthanized and the tumors were weighed. The statistical significance was determined by using the analysis of variance of the P value ($^*P < 0.05$, $^{**}P < 0.01$).

2.14 H&E staining and caspase-3 staining

To further compare and characterize the difference of phototherapy efficiency under 808 and 1064 nm irradiation, the tumors were removed after finishing the experiment. The typical tumors of the mice in the six groups (I: PBS; II: PBS + 808 nm laser, III: PBS + 1064 nm laser, IV: PEG-MoO_x NPs, V: PEG-MoO_x NPs + 808 nm laser, VI: PEG-MoO_x NPs + 1064 nm

laser) were harvested for haematoxylin and eosin (H&E) staining and histopathological analysis. Caspase-3 immunohistochemical staining was also performed to measure the extent of the apoptosis of the tumors. The slices of the tumors were examined with an inverted fluorescence microscope.

2.15 Characterization

Transmission electron microscopy (TEM) and high-resolution transmission electron microscopy (HR-TEM) of the samples were performed using a FEI Tecnai G2 S-Twin system with a field emission gun operating at 200 kV. The element analysis of the samples was performed using an energy-dispersive X-ray spectrum (EDX, HORIBA EMAX-250) attached on a field emission scanning electron microscope (FE-SEM) (S-4800, Hitachi, Japan). X-ray powder diffraction (XRD) analysis was performed using a Japan Rigaku D/max-2500 diffractometer with Cu Kα radiation (λ = 1.5418 Å). X-ray photoelectron spectroscopy (XPS) was performed on a Kratos AXIS-165 surface analysis system. Dynamic light scatting (DLS) data were provided by using a Nicomp380 ZLS plus ZETADi system. The UV-vis-NIR data were obtained by using a U-3900 spectrophotometer (Hitachi). The Fourier transform infrared (FT-IR) spectrum was recorded on an infrared microscope (iN10-IZ10, Thermo Fisher). Infrared thermal imaging was acquired at different irradiation times and recorded using a FLIR thermal camera (FLIR ThermaCAM E40). Inductively coupled plasma-mass spectrometry (ICP-MS) was conducted using an iCAP 6300 system (Thermo Scientific).

2.16 Statistical analysis

All data are expressed in this article as mean result ± standard deviation (SD). The statistical analysis was performed with Origin 8.5 software.

3. Results and discussion

3.1. Physical and chemical characterization of PEG-MoO_x NPs

Scheme 1 demonstrates the synthetic process of PEGylated MoO_x nanoparticles (PEG-MoO_x NPs) and their potential use as phototherapeutic agents in the NIR-II window. First, $(NH_4)_6Mo_7O_{24}{\cdot}4H_2O$ was hydrolyzed in a mixture of water–ethanol solution, whose pH was adjusted to 1.2 with hydrochloric acid before a hydrothermal process at 160 °C for 12 h. We find that the morphology of the MoO_x is nanoparticles with a diameter range from 15 to 30 nm in a transmission electron microscopy (TEM) image (Fig. 1a). The spacing between the adjacent lattice planes corresponds to the *d*-spacing of (010) planes and is 0.334 nm as provided by a high-resolution TEM (HR-TEM) image (Fig. 1b). In addition, given that dynamic light scattering (DLS) is an effective tool to determine the hydrodynamic diameter and dispersity of NPs, we investigated the hydrodynamic diameter of PEG-MoO_x NPs in distilled water. According to the DLS measurement result (Fig. 1c), the hydrodynamic diameter of PEG-MoO_x NPs ranges

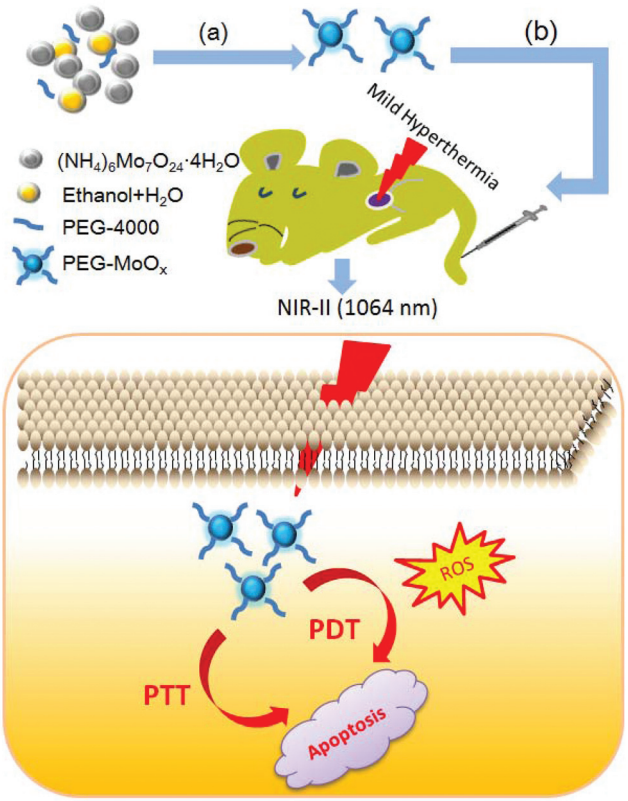

Scheme 1 Schematic illustration for the (a) synthesis of PEG-MoO_x NPs and (b) NIR-II 1064 nm laser induced synergetic PTT and PDT of tumors under mild hyperthermia conditions.

from 25 to 40 nm, suggesting a good dispersion of these NPs in water. The X-ray diffraction (XRD) pattern was used to characterize the crystal structure of the sample (Fig. 1d). The XRD pattern reveals that the diffraction peaks can be assigned to a mixture of orthorhombic Mo_4O_{11} (JCPDS no. 65-0397, marked with ♣) and monoclinic MoO_2 phases (JCPDS no. 65-1273, marked with ♤).[34] Energy dispersive X-ray spectrum (EDX) analysis detected the element distribution of molybdenum, oxygen, and carbon in the PEG-MoO_x NPs (Fig. S1a†) and no other impurities were detected, revealing a high phase purity of the product. X-ray photoelectron spectroscopy (XPS) measurement was further carried out to determine the valence state of Mo in the PEG-MoO_x NPs (Fig. 1e and f). In the high-resolution XPS spectrum of Mo 3d and curve fitting data in Fig. 1f, the main peaks at 229.6 and 232.8 eV can be attributed to the binding energies of Mo $3d_{5/2}$ and Mo $3d_{3/2}$ of Mo^{4+}.[35] The weak peaks located at 234.8 and 231.7 eV were assigned to the Mo $3d_{3/2}$ and Mo $3d_{5/2}$ of Mo^{5+}, respectively.[36] In addition, the binding energy values at 233.5 eV for the Mo $3d_{3/2}$ level and 236.8 eV for the Mo $3d_{5/2}$ level were observed, which correspond to the standard values of Mo^{6+} reported in the literature.[37] By calculating the area ratio of Mo^{6+}, Mo^{5+}, and Mo^{4+} from the XPS spectra, we can conclude that PEG-MoO_x NPs contain 22.0% Mo^{6+}, 42.6% Mo^{5+}, and 35.4% Mo^{4+}, respectively. This result indicated that

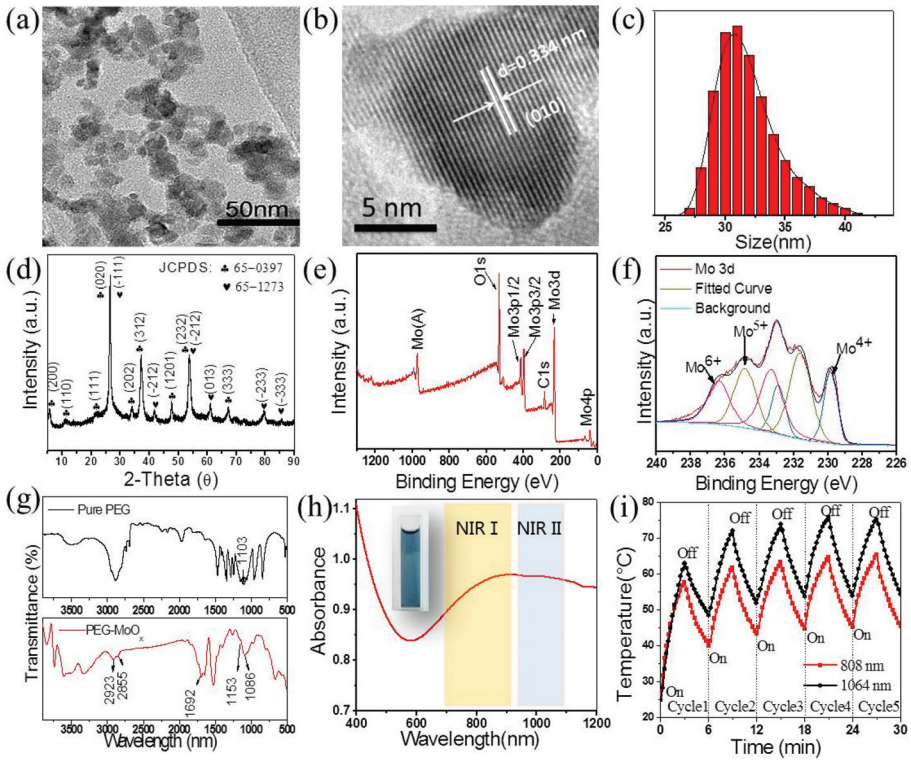

Fig. 1 (a) TEM image, (b) HR-TEM image, and (c) DLS pattern of PEG-MoO_x NPs (concentration: 50 μg mL^{-1}). (d) XRD pattern of PEG-MoO_x NPs. A survey XPS spectrum (e) and a Mo 3d core level spectrum (f) of PEG-MoO_x NPs. (g) FI-IR spectra of pure PEG and PEG-MoO_x NPs. (h) UV-vis-NIR absorbance spectrum of the PEG-MoO_x NPs aqueous solution. The inset in (h) shows the photograph of the PEG-MoO_x aqueous solution. The NIR I and II biological windows are indicated by yellow and blue bars. (i) Five cycles of NIR laser irradiation were performed for concentrations of 1.0 mg mL^{-1} of the PEG-MoO_x NPs aqueous solution. Each cycle consisted of 3 min irradiation followed by a 3 min cooling phase (power density: 1.0 W cm^{-2}).

oxygen-deficient molybdenum oxides are formed, which is in agreement with the XRD result. The Fourier transform infrared (FT-IR) spectrum (Fig. 1g) reveals that peaks associated with the asymmetric and symmetric stretching vibrations of methylene units (–CH_2– groups) are at 2923 and 2855 cm^{-1}, respectively. Compared with the FT-IR spectrum of pure PEG in Fig. 1g, the characteristic stretching vibration of the C–O–C group at 1103 cm^{-1} shifted to a lower wavenumber,[38,39] suggesting that the PEG has been successfully modified onto the surface of MoO_x NPs. It was reported that MoO_x with a mixed valence state of Mo^{4+}, Mo^{5+}, and Mo^{6+} could be oxidized into Mo^{6+} in the presence of oxygen.[40] Therefore, we investigated the stability of PEG-MoO_x NPs in phosphate buffered saline (PBS) (pH = 7.4) for a prolonged incubation time. TEM images in Fig. S1b and c† indicate that the sizes of the PEG-MoO_x NPs decreased to ~5 nm within 48 h. And almost no large NPs except for many ultrasmall particles (less than 5 nm) were observed after 72 h. At the same time, the blue NP solution became almost colorless, further suggesting a gradual degradation of the NPs in the PBS solution (Fig. S2a†). Moreover, we also found that there was no visible color change of the PEG-MoO_x NPs after being incubated with acidic PBS buffer (pH = 5.0) within 72 h as shown in Fig. S2a.† Therefore, it can be concluded that the PEG-MoO_x NPs are pH-responsive to the physiological environment. Furthermore, we performed XPS to testify the product during the degradation process. As shown in Fig. S2b and c,† the XPS spectra revealed that Mo^{4+} in the original sample (Fig. 1f) disappeared completely and Mo^{6+} increased after being incubated in PBS buffer at pH 7.4 for 48 h, and then Mo^{5+} decreased quickly and the concentration of Mo^{6+} increased from 20% to 80% when the incubation time was prolonged to 72 h, indicating that most of the Mo^{5+} was oxidized to Mo^{6+} for those NPs at the physiological pH value. For the formula of Mo(VI), we propose as follows: small H^+ ions in the reactant could partially react with the MoO_x (x = 4, 5, 6), forming $H_x(Mo^V_x)(Mo^{VI}_{1-x})O_3$.[40] In our experiment, $H_x(Mo^V_x)(Mo^{VI}_{1-x})O_3$ could be neutralized by the weak alkali PBS buffer (pH 7.4) to form $[Mo^V_x(Mo^{VI}_{1-x})O_3]^-$, which is then oxidized into $[Mo^{VI}O_4]^{2-}$. However, $H_x(Mo^V_x)(Mo^{VI}_{1-x})O_3$ is very stable under acidic conditions and the oxidation of Mo^V was very slow.

The UV-Vis-NIR spectrum in Fig. 1h shows the extended NIR absorption of PEG-MoO_x NPs that covers the NIR-I and NIR-II biological windows. The remarkable photo-absorption of PEG-MoO_x NPs motivated us to evaluate the photothermal conversion effect. Two different lasers (808 nm, 1064 nm) were used to irradiate PEG-MoO_x NPs with different concentrations at a power density of 1.0 W cm^{-2} for 600 s. The temperature

change trends during the heating or cooling process of the PEG-MoO_x solutions were recorded with a FLIR thermal camera (Fig. S5†). Observably, the temperature of the aqueous dispersion of PEG-MoO_x NPs increased under the 808 and 1064 nm laser irradiation (Fig. S3a, b and S4a, b†). For example, at 200 μg mL^{-1}, the temperature of the PEG-MoO_x aqueous dispersion increased from 25.0 °C to 54.5 °C under 1064 nm NIR irradiation for 600 s, while, under the same conditions, it increased to 43.1 °C under 808 nm laser irradiation. Water was set as the control and the slight temperature change induced by water can be ignored under 808 or 1064 nm irradiation. The temperatures of all the PEG-MoO_x NPs solutions increased rapidly and showed a concentration-dependent increase, indicating that the NPs could efficiently convert NIR laser energy into heat. Moreover, the photothermal conversion efficiency of the NPs was quantified to be 27.3% (808 nm irradiation) and 37.4% (1064 nm irradiation) by the NIR laser heating–cooling cycle (ESI, Fig. S3c, d and S4c, d†). We also tested the photo-stability of PEG-MoO_x NPs (reproducibility of the heating process) *via* 808 nm and 1064 nm laser irradiation. Five cycles of NIR laser irradiation were performed for concentrations of 1.0 mg mL^{-1}. Each cycle consisted of 3 min irradiation followed by a 3 min cooling phase (Fig. 1i). By repeating the laser on–off cycles, the temperature at each step increases slightly without compromising the photothermal efficiency significantly. Thus, the as-prepared PEG-MoO_x NPs as a photothermal nanoagent can overcome the limitation of the loss of NIR absorbance after irradiation and hence maintained their good photothermal conversion efficacy compared with the Au nanoagent.[41]

3.2. Extracellular ROS detection

PDT requires an effective production of reactive oxygen species (ROS) at the tumor site.[42] In order to verify the capability of PEG-MoO_x NPs to produce ROS under NIR laser irradiation, an experiment using a 1,3-diphenylisobenzofuran (DPBF) probe as an acceptor of $^1O_2$ (a typical ROS) was carried out.[43,44] As shown in Fig. 2a, there is no noticeable absorption change of the DPBF + 1064 nm laser and DPBF + PEG-MoO_x NPs without 1064 nm laser irradiation. However, $^1O_2$ was produced immediately following the 1064 nm irradiation of PEG-MoO_x NPs by its reaction with DPBF, resulting in the decreased absorption of DPBF at 410 nm. In addition, after the 1064 nm irradiation of the NPs, the amount of the generated $^1O_2$ increased depending on the irradiation time (Fig. 2b). In contrast, the 808 nm NIR irradiation did not cause a clear decrease of DPBF's absorption at 410 nm within the irradiation time (Fig. 2c and d). Therefore, it can be concluded that PEG-MoO_x NPs under 1064 nm laser irradiation can result in a clear decay of DPBF due to the continuous generation of $^1O_2$. In general, the mechanisms of ROS production of plasmonic nanomaterials under NIR irradiation are very complicated.[45] We speculated the $^1O_2$ production mechanism of the photothermal PEG-MoO_x nanoagent as follows: it has been reported that one of the plasmon-activated pathways proceeds mainly *via* an indirect photothermal process for plasmonic

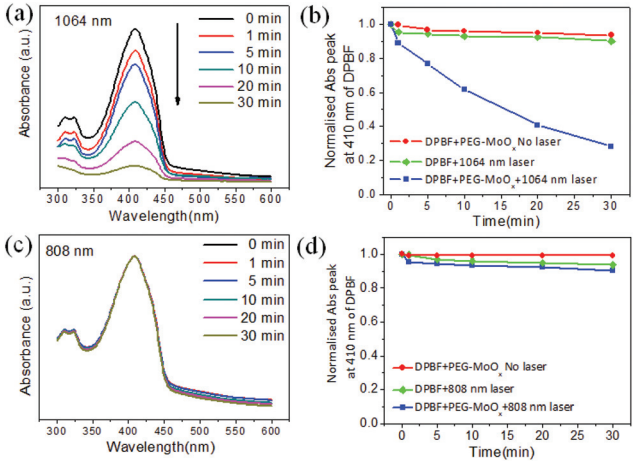

Fig. 2 Investigation of the generation of reactive oxygen species (ROS). UV-Vis absorption spectra of the DPBF solution incubated with PEG-MoO_x NPs under (a) 1064 nm and (c) 808 nm irradiation for different times; UV-Vis absorption at 410 nm of DPBF incubated with PEG-MoO_x NPs as a function of (b) 1064 nm and (d) 808 nm laser irradiation time (power density for 1064 nm: 1.0 W cm^{-2}, power density for 808 nm: 1.2 W cm^{-2}).

nanomaterials under NIR laser irradiation that induces extreme heat development leading to particle fragmentation and increased thermionic electron emission.[18,46] The remarkable distinction in $^1O_2$ production under the two different NIR-I and NIR-II windows could be justified on the grounds of heat generation based on the different photothermal conversion abilities. The photothermal conversion efficiency under the 1064 nm irradiation is much higher than those at the wavelength of 808 nm when the power density was set at 1.0 W cm^{-2}, which has been proved in Fig. S3–S5.† The higher temperature of the PEG-MoO_x NPs solution under the 1064 nm irradiation could be the main reason for the clear $^1O_2$ production compared with that under the 808 nm irradiation during the photothermal therapy. However, at the same power density, the relatively low temperature produced by the 808 nm irradiation was not enough to increase the thermionic electron emission. The detailed mechanism for such an excitation wavelength dependent ROS production of MoO_x-PEG still requires further detailed study in the future.

3.3. *In vitro* cytotoxicity, phototherapy and intracellular ROS detection

Efficient cell entry is a prerequisite for the PEG-MoO_x NPs to function as phototherapy agents. Therefore, cell uptake was assessed with HeLa cells (a human cervical carcinoma cell line) cultured in 24-well culture plates. The concentrations of PEG-MoO_x NPs were 6.25, 25, and 100 μg mL^{-1}. The intracellular Mo content was measured by inductively coupled plasma mass spectrometry (ICP-MS) following incubation for different times (2, 6, and 24 h). As can be seen in Fig. 3a, intracellular Mo content shows increasing uptake with increasing concentration and time. Next, the biocompatibility was investigated.

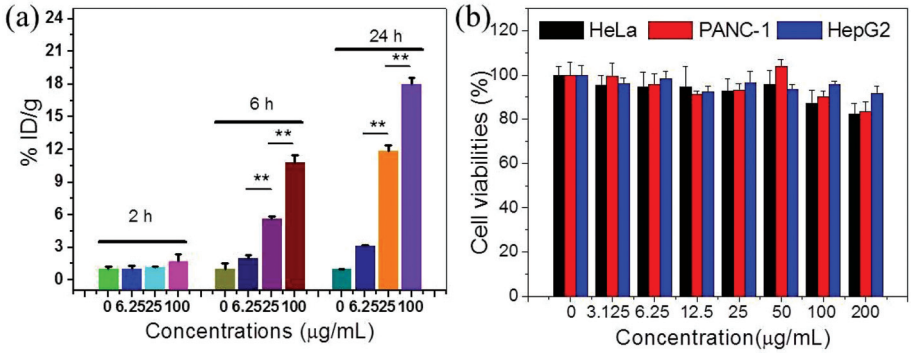

Fig. 3 (a) Cellular uptake of PEG-MoO_x NPs after incubation with HeLa cells for 2, 6, and 24 h. (b) Cell viabilities of HeLa, PANC-1 and HepG2 cells treated with PEG-MoO_x NPs for 24 h.

The standard CCK-8 assay with the PEG-MoO_x NPs was performed on HeLa, HepG2, and PANC-1 cells. As illustrated in Fig. 3b, the cell viabilities of the three different cell lines can reach above 82% after incubation with these NPs up to a concentration of 200 μg mL^{-1}.

In Fig. 4a and Fig. S5,† to demonstrate that PEG-MoO_x NPs can act as NIR activatable nanoagents at the cellular level, the HeLa, PANC-1, and HepG2 cells were incubated with the PEG-MoO_x NPs at 37 °C and irradiated with NIR 808 nm (1.2 W cm^{-2}, 10 min) and 1064 nm (1.0 W cm^{-2} for 10 min) lasers (the maximum temperature control was maintained at 43 °C under the two laser irradiation). Because the laser-caused hyperthermia for cancer treatment is nonspecific, it is necessary to choose appropriate laser parameters to obtain an effective phototherapeutic response and simultaneously ensure laser illumination safety to the surrounding normal tissues.[47] In our experiments, the cell viabilities of the control groups are 89% and 87% after 10 min of NIR laser irradiation, demonstrating that the used power densities (1.2 W cm^{-2} for 808 nm and 1.0 W cm^{-2} for 1064 nm) do not damage the HeLa cells. Consequently, compared with the control group, a clear drop in the percentage of cell viabilities in a dose-dependent

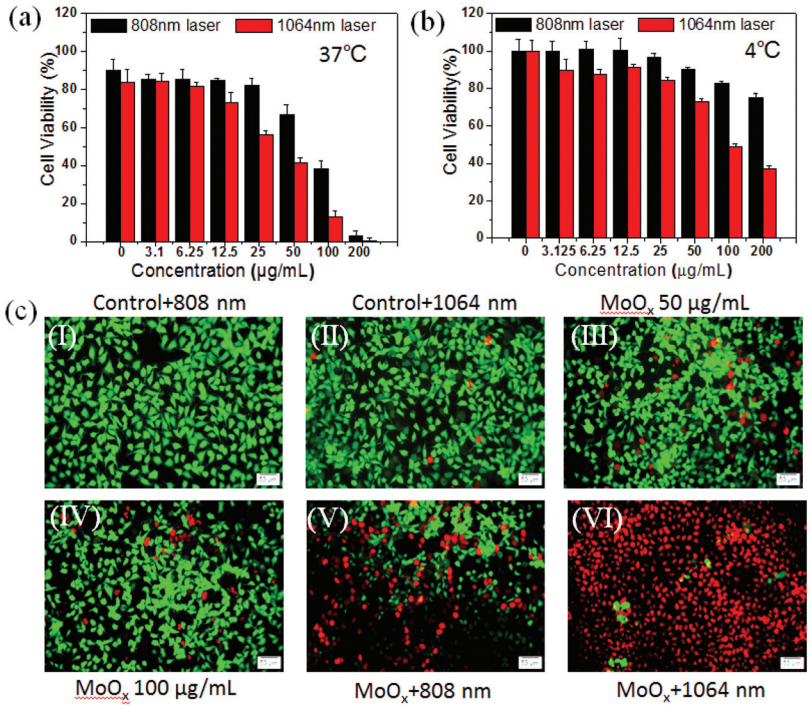

Fig. 4 Comparison of the cell viability of HeLa cells incubated with PEG-MoO_x NPs under 808 nm and 1064 nm laser irradiation at an environmental temperature of (a) 37 °C and (b) 4 °C. (c) Fluorescence images of HeLa cells after co-staining using CA/PI: (I) Control + 808 nm, (II) Control + 1064 nm laser, (III) PEG-MoO_x NPs (50 μg mL^{-1}). (IV) PEG-MoO_x NPs (100 μg mL^{-1}), (V) PEG-MoO_x NPs (100 μg mL^{-1}) + 808 nm laser (power density: 1.2 W cm^{-2}, the maximum temperature control at 43 °C), (VI) PEG-MoO_x NPs (100 μg mL^{-1}) + 1064 nm laser (power density: 1.0 W cm^{-2}, the maximum temperature control at 43 °C) (scale bar: 50 μm).

manner occurs in the two groups upon exposure to 808 nm and 1064 nm lasers. In particular, irradiation with the 1064 nm laser resulted in much lower cell viabilities than those irradiated with the 808 nm laser (13% *vs.* 38% cell viabilities at the concentration of 100 μg mL^{-1}) as shown in Fig. 4a. To better elucidate the phototherapy effect, a systematic study was carried out. As shown in Fig. 4b, when the medium temperature was lowered from 37 °C to 4 °C to avoid the mild hyperthermia induced by the two NIR lasers, high cell viability was observed for the HeLa cells irradiated with the 808 nm laser and then incubated with the NPs for 24 h. At the concentration of 100 μg mL^{-1} of the NPs, the viability of the 808 nm laser irradiated cells can reach 83% while it clearly decreased to 49% upon 1064 nm photoirradiation at 4 °C, implying that 1064 nm irradiation can lead to greater cytotoxicity. Moreover, it is well understood that the photothermal effect can be significantly suppressed by lowering the medium temperature from 37 to 4 °C. Next, live/dead staining using calcein AM/PI was conducted using HeLa cells to further investigate the cytotoxicity of PEG-MoO_x NPs with or without NIR laser exposure (Fig. 4c). It was noteworthy that the cell viability was not influenced by PEG-MoO_x NPs with concentrations up to 100 μg mL^{-1}, verifying that the NPs possess low cytotoxicity. In contrast, many more dead cells (red color) were detected in the group of PEG-MoO_x NPs + 1064 nm compared with those irradiated with the 808 nm laser, suggesting that PEG-MoO_x

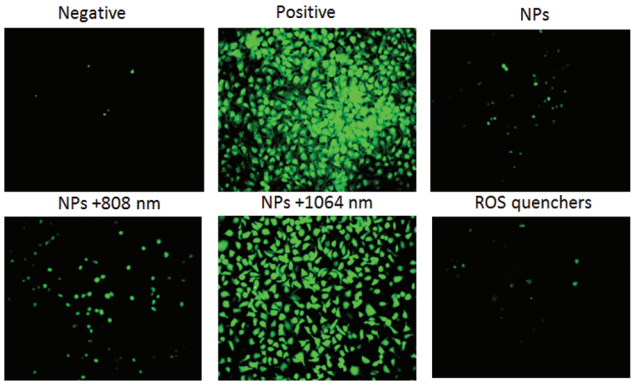

Fig. 5 Comparison of the NIR laser irradiation of PEG-MoO_x NPs treated HeLa cells that causes oxidative stress detected by the ROS probe DCFH-DA, which emits green fluorescence when oxidized by ROS. The HeLa cells were incubated with PEG-MoO_x NPs with/without 808 and 1064 nm laser irradiation. ROS was quenched by ROS quenchers (histidine and mannitol) after the incubation of the cells with PEG-MoO_x NPs under 1064 nm laser irradiation. The irradiation time was set at 10 min.

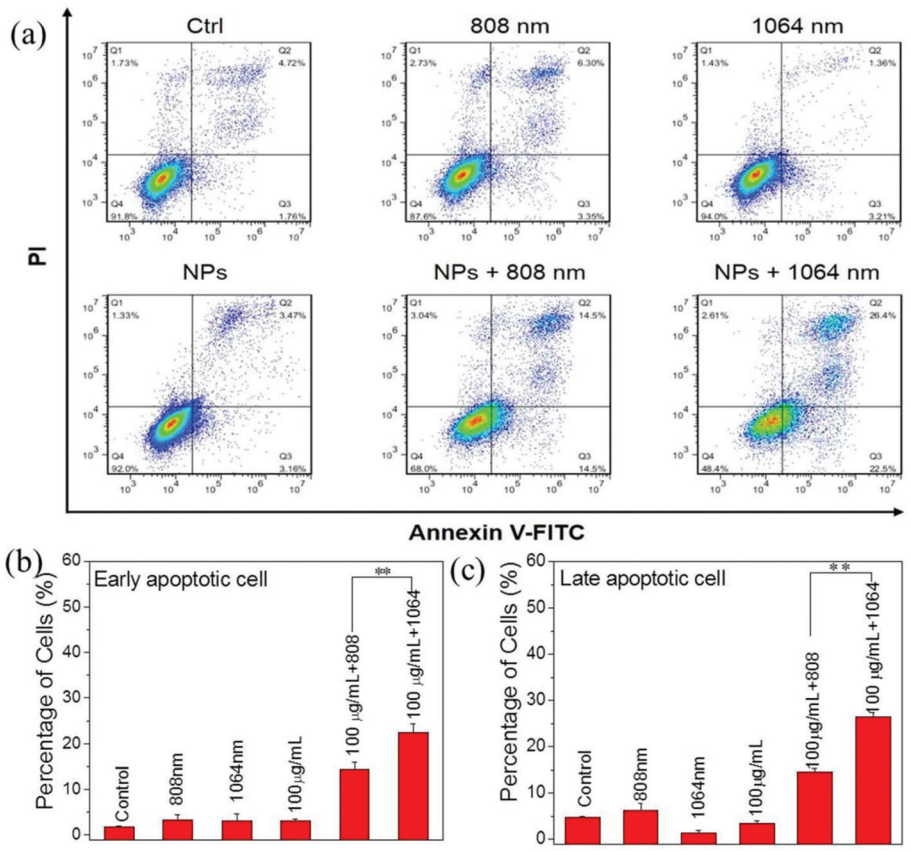

Fig. 6 (a) Flow cytometric profiles of HeLa cells were conducted to determine the percentages of early apoptosis and late apoptosis/necrosis cells with different treatments. Control, Control + 808 nm, Control + 1064 nm, PEG-MoO_x NPs (100 μg mL^{-1}), PEG-MoO_x NPs + 808 nm, PEG-MoO_x NPs + 1064 nm (power density of 808 nm laser: 1.2 W cm^{-2}; power density of 1064 nm laser: 1.0 W cm^{-2}; irradiation time: 10 min). (b, c) Statistical data of the percentage of early apoptosis and late apoptosis cells under different treatments.

NPs under 1064 nm irradiation can cause more effective phototherapy on HeLa cells.

To further verify the difference in the photo-responsive properties and the capability of PEG-MoO_x NPs upon 808 and 1064 nm irradiation, dichlorofluorescein diacetate (DCFH-DA) is applied to assess the intracellular ROS levels. In the presence of ROS, DCFH-DA is oxidized into fluorescent dichlorofluorescein (DCF) in live cells, which emits bright green fluorescence.[48] The formation of ROS in HeLa cells after incubation with PEG-MoO_x NPs sensitized by NIR laser irradiation was assessed by using the DCFH-DA probe. It can be found that more intense green fluorescence could be detected in the PEG-MoO_x NPs + 1064 nm group than in the other groups (Fig. 5) when all the fluorescent images were collected at the same setting. A quantitative comparison of ROS generation and quenching from the mean fluorescence intensity of DCF in Fig. S6† demonstrates that the intensity of the PEG-MoO_x NPs + 1064 nm group was nearly 3 times higher than that of the PEG-MoO_x NPs + 808 nm group. The use of ROS quenchers (histidine and mannitol) for the PEG-MoO_x NPs upon irradiation at 1064 nm further indicated that higher amounts of ROS were quenched in the HeLa cells (Fig. 5 and Fig. S6†). On the basis of the above findings, we can conclude that cellular death of the HeLa cells upon 808 nm irradiation is most probably due to the PTT effect, whereas the improved therapy effect upon 1064 nm irradiation could be attributed to the great contribution of ROS-mediated PDT combined with PTT.

To further make sure the cell death mechanism after the phototherapy in the NIR-II window, flow cytometry was performed by using annexin-V-FITC/PI as the probe. Fig. 6 shows the flow cytometry data of the HeLa cells treated with PEG-MoO_x NPs with and without laser irradiation. The annexin-V-FITC emission signal was plotted on the *x*-axis, while the PI emission signal was plotted on the *y*-axis. The quantities of living cells, early apoptosis cells, and late apoptosis/necrosis cells were determined. In Fig. 6, 87%–83.9% of cell viabilities were observed in the NIR treated group and the PEG-MoO_x NP treated group. However, the early apoptosis rate of the cells can reach 14.5%, and the late apoptosis/necrosis rate was 17.54% after the 808 nm irradiation of PEG-MoO_x NPs with the concentration of 100 μg mL^{-1}. In contrast, after 1064 nm laser irradiation, the early apoptosis rate of the cells reached 22.5%, and the late apoptosis/necrosis rate was 48.9%. Quantitatively, the amount of cellular apoptosis and necrosis (71.4% *vs.* 32.04%) induced by 1064 nm irradiation was approximately 2.2 times higher than those treated upon 808 nm irradiation of 100 μg mL^{-1} of the PEG-MoO_x NPs. Therefore, the flow cytometry further evidences the synergistic effect of the PDT and PTT of PEG-MoO_x NPs under 1064 nm irradiation, which is in agreement with the results shown in Fig. 4.

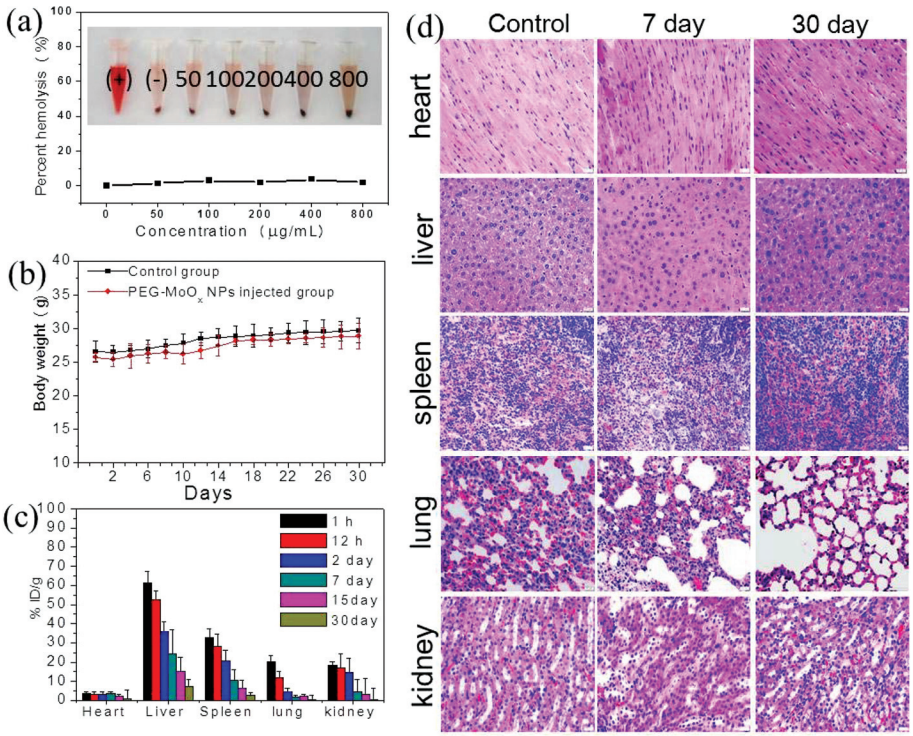

Fig. 7 (a) Hemolytic percentage of RBCs incubated with PEG-MoO_x NPs at various concentrations, and deionized water (+) and PBS (–) as the positive and negative controls, respectively. Inset: Photographs for the direct observation of hemolysis, showing that PEG-MoO_x NPs exhibit good biocompatibility. (b) Time evolution of the averaged weight (n = 3 for each group) within 30 days after the i.v. injection of PEG-MoO_x NPs to mice *via* the tail vein. (c) ICP-MS quantitative measurement of Mo concentrations in each organ of the mice after the i.v. injection of PEG-MoO_x NPs (dosage: 20 mg kg^{-1}) at different times post-injection. (d) Photos of H&E stained tissue sections to monitor the histological changes in the heart, liver, spleen, lung, and kidney of mice after the i.v. injection of PEG-MoO_x NPs with different time treatments (scale bar: 20 μm).

3.4. *In vivo* toxicity assessment and biodistribution

To further evaluate their biocompatibility, we investigated the influence of PEG-MoO_x NPs on the hemolytic behavior of red blood cells (RBCs), where deionized water and PBS were used as the positive and negative control, respectively (Fig. 7a). These results showed that at a concentration below 200 μg mL^{-1}, no clear hemolytic RBCs (<2.1%) were detected. Next, the *in vivo* toxicity assessment and biodistribution investigation were conducted by intravenously (i.v.) injecting PEG-MoO_x NPs at a dosage of 20 mg kg^{-1} into the tail vein of healthy male BALB/c mice. The body weights of the i.v. injected mice were also measured. As shown in Fig. 7b, the change of the body weight of the mice treated with PEG-MoO_x NPs (2 mg mL^{-1}, 200 μL per mice) was similar to that of the control group, indicating that the PEG-MoO_x NPs have no evident toxic effect on mice within 30 days. In addition, no infection and reduced food taking were observed in the mice. Meanwhile, after the mice were injected through the tail vein, all the major organs were surgically removed from the mice at time intervals of 1 h, 12 h, 2 days, 7 days, 15 days, and 30 days. The Mo concentrations in these organs were measured by ICP-MS (Fig. 7c). As depicted in Fig. 7c, early accumulation within 12 h predominantly in the liver, spleen, and lung is expected and is related to the clearance of the NPs from the blood by the cells of the mononuclear phagocytic system.[49] The accumulation in the kidney is also high within 12 h. Then, after 2 days, the amount of Mo element in the liver, spleen, and lung decreased quickly with prolonged time. Most of the NPs were excreted from the liver and spleen post-injection and the Mo element level in all the examined organs became very low. This result could be attributed to the gradual

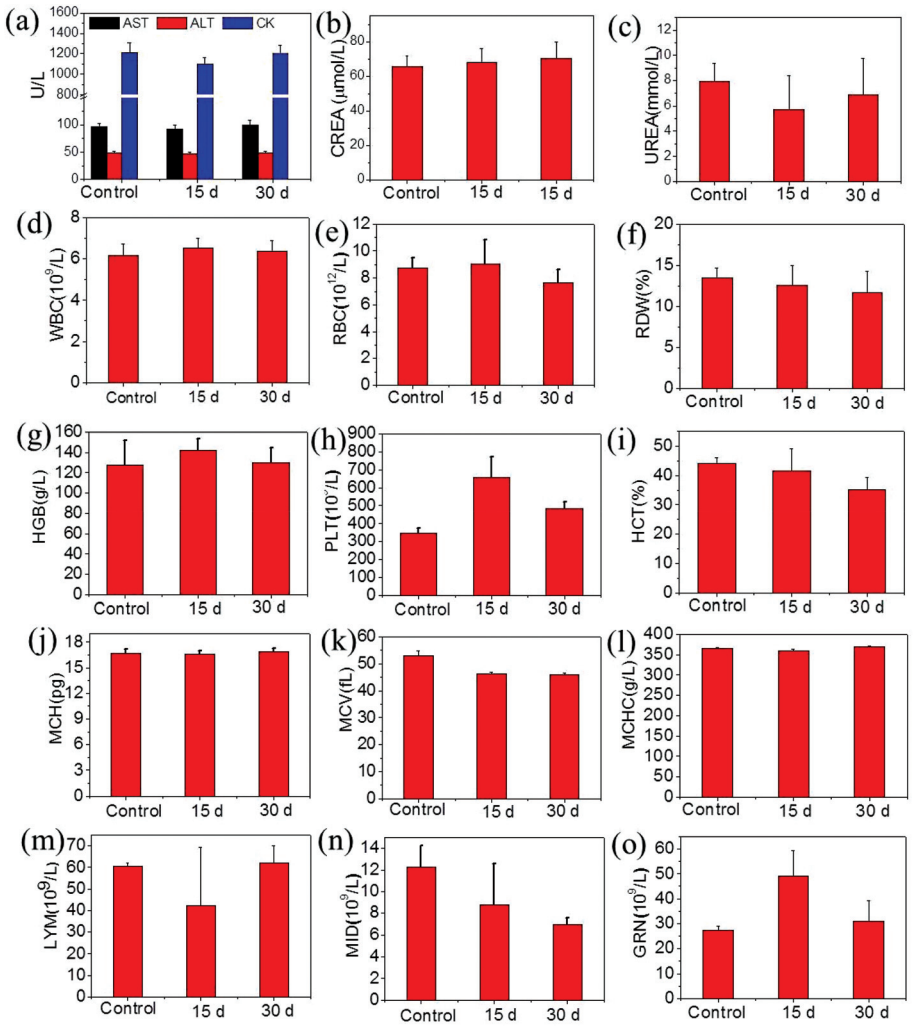

Fig. 8 (a–c) Serological analysis of BALB/c mice after the i.v. injection of PEG-MoO_x within 30 days. (d–o) Haematological routine data of BALB/c mice treated with PEG-MoO_x after the i.v. injection within 30 days. Error bars represent the standard deviation calculated from three mice. Untreated mice were used as the control. (d) White blood cells (WBC), (e) red blood cells (RBC), (f) red cell distribution width (RDW), (g) hemoglobin (HGB), (h) platelet (PLT), (i) hematocrit (HCT), (j) mean corpuscular hemoglobin (MCH), (k) mean corpuscular volume (MCV), (l) mean corpuscular hemoglobin concentration (MCHC), (m) lymphocytes (LYM), (n) minimum inhibitory dilution (MID), and (o) granulocytes (GRN).

oxidation and degradation of the MoO_x NPs into ultrasmall NPs and $[Mo^{VI}O_4]^{2-}$ at the normal physiological pH of 7.4, which were consequently filtered *via* the kidneys *in vivo*.

Next, the histological examination of the major organs excised from the PEG-MoO_x NP injected mice at different post-injection time points was carried out using haematoxylin and eosin (H&E) staining analysis. Notably, the structures of the organs (heart, liver, spleen, lung, and kidney) from the exposed mice were normal, hardly different from those of the control group. No pathological abnormality such as necrosis or inflammatory response to the examined organs was observed within the tested time (Fig. 7d). The toxicity of PEG-MoO_x NPs was also assessed by the biochemical analysis of the mice on the 7th day and 30th day post-intravenous administration. The main liver function and kidney function markers including the alanine aminotransferase (ALT), aspartate aminotransferase (AST), creatine kinase (CK), creatinine (CREA), and urea (UREA) indicators were all measured. Encouragingly, these parameters fell within the normal reference ranges compared with the control group (Fig. 8a–c), suggesting no clear hepatic and kidney toxicity of mice injected with PEG-MoO_x NPs. A routine blood examination was performed including white blood cells (WBC), red blood cells (RBC), red cell distribution width (RDW), hemoglobin (HGB), platelet (PLT), hematocrit (HCT), mean corpuscular hemoglobin (MCH), mean corpuscular volume (MCV), mean corpuscular hemoglobin concentration (MCHC), lymphocytes (LYM), minimum inhibitory dilution (MID), and granulocytes (GRN) (Fig. 8d–o). These hematological analyses show that all these parameters were also similar to the control groups within the test period. Therefore, we can predict that the PEG-MoO_x NPs have good biocompatibility *in vivo*.

3.5. *In vivo* phototherapy of tumor under 1064 nm irradiation

It is reasonable to expect that the high photothermal conversion efficiency, effective ROS generation under 1064 nm irradiation, and good biocompatibility make the low cost plasmonic PEG-MoO_x NPs a powerful nanoplatform for tumor therapy *in vivo*. For *in vivo* phototherapy, we chose a PANC-1 tumor-bearing mice model. As has been reported, controlled localized temperature increments (within the range of 42–43 °C) have shown enhanced signs of apoptosis on tumor cells in the PTT process, which is beneficial to kill tumor cells.[50] Therefore, we utilized mild hyperthermia to kill cancer cells. Firstly, PANC-1 tumor-bearing mice were randomly divided into six groups. Then, Group I as the control received PBS injections only, while Groups II and III received intravenous PBS injection but were exposed to the 808 nm and 1064 nm laser, respectively. PEG-MoO_x NPs was i.v. injected to the mice of Groups IV, V, and VI. We further investigated the phototherapy efficacies of these i.v. injected PEG-MoO_x NPs in the PANC-1 tumor model (n = 3 per group). At 1 h post-injection, the tumor of each mouse (Groups V and VI) was irradiated with the 808 nm and 1064 nm NIR laser (808 nm laser, 0.75 W cm^{-2}; 1064 nm laser, 0.6 W cm^{-2}), respectively, for 10 min and the temperature in both the groups was maintained near ~43 °C (Fig. 9a and b). The images were analyzed using an FLIR thermal camera to obtain the average temperature of the tumor. As shown in Fig. 9a, for the PEG-MoO_x NPs + NIR laser groups,

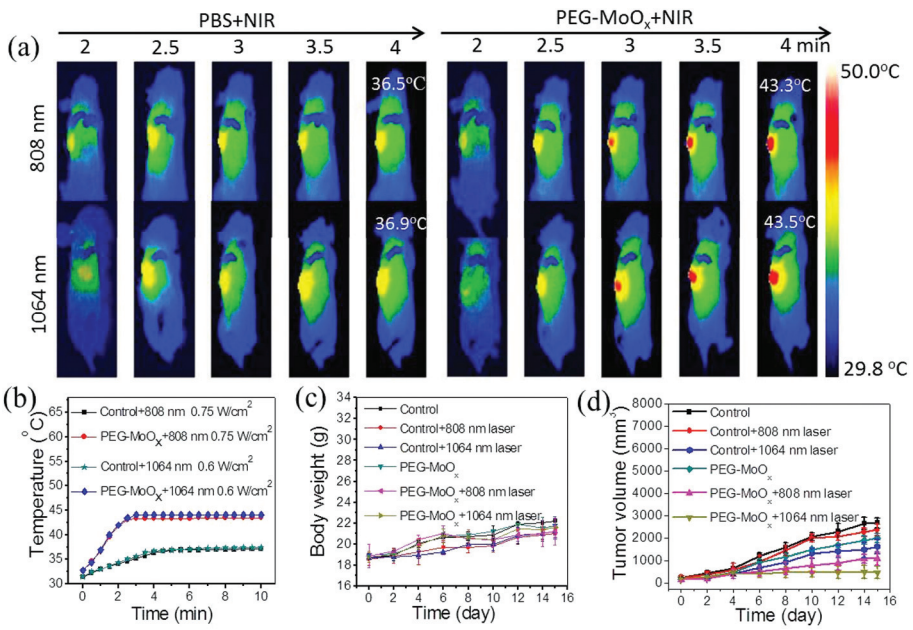

Fig. 9 (a) Infrared thermal images of tumor-bearing mice after treatment with PBS + 808 nm, PBS + 1064 nm, PEG-MoO_x + 808 nm, PEG-MoO_x + 1064 nm (power density of the 808 nm laser: 0.75 W cm^{-2}; power density of the 1064 nm laser: 0.60 W cm^{-2}). (b) Tumor temperatures of mice monitored with an infrared thermal camera as a function of irradiation time. (c) Body weights of tumor-bearing mice in different groups. (d) Tumor volume in different groups measured every two days.

thermal images recorded at different time points indicated that the temperature of the tumor region quickly increased and then reached a plateau upon laser irradiation. The temperature could easily reach a level of ~43.3 °C (ΔT = 13 °C) and is capable of inducing a mild hyperthermia to kill cancer cells (Fig. 9b). However, no noticeable temperature rise in the control group injected with PBS was observed.

The body weights and tumor volumes were monitored every two days (Fig. 9c and d). The body weights of all the six groups appeared variable but showed an overall growth trend. Clear differences occurred in the change of tumor volumes, as can be seen in Fig. 9d, after 15 days; the tumor volumes of Groups I, II, III, and IV showed extraordinary growth, while Group V and VI showed tumor volumes about 700 mm^3 and less than 190 mm^3, respectively (Fig. S8†). On the 15th day, the mice were euthanized and the tumors were weighed (Fig. 10a).

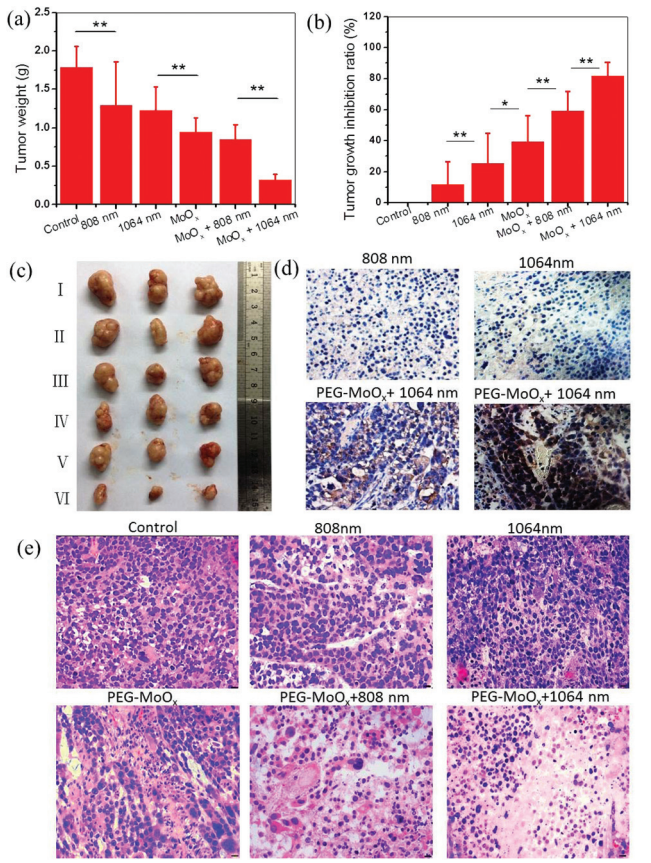

Fig. 10 (a) Tumor weight for each group after the mice were sacrificed and tumors were removed on the 15th day. (b) Tumor growth inhibition ratio in different treatment groups. (The statistical significance was determined by using the analysis of variance (*P* value). (*P < 0.05, **P < 0.01.) (c) Photographs of mice in the different treatment groups on the 15th day. Group I: Control (PBS), Group II: PBS + 808 nm laser, Group III: PBS + 1064 nm laser, Group IV: PEG-MoO_x NPs, Group V: PEG-MoO_x NPs + 808 nm laser, Group VI: PEG-MoO_x NPs + 1064 nm laser. (d) Caspase-3 stained images of tumors with different treatments. (e) H&E stained histological images of the tumors after different treatments (scale bar: 40 μm; error bars were calculated based on triplicated samples).

Group VI has the minimal tumor weight of ~0.25 g compared with the other groups. In addition, the mice treated with the 808 nm laser irradiated PEG-MoO_x NPs show 59.31% of the tumor growth inhibition ratio, while the mice treated with 1064 nm laser irradiation show 82.44% of the tumor growth inhibition ratio (Fig. 10b). Remarkably, after 15 days of treatment in Group VI, the skin of the mice at the irradiation site was undamaged but tumor growth was effectively inhibited under mild hyperthermia. The digital photos of the excised tumors in Fig. 10c show that the tumor size for the mice treated with PEG-MoO_x NPs under 1064 nm laser irradiation is the smallest, confirming an enhanced permeability and retention (EPR) effect as the main cause of the highly passive tumor uptake of the NPs and an efficient tumor inhibition effect attributed to the synergetic PTT and PDT. Moreover, the change in the tumor volumes and weights of only the NIR irradiation groups (Groups II and III) reveals little inhibitory effects on the growth of tumors, demonstrating the negligible thermal damage by the NIR laser. In brief, these results illustrate that the combination of PTT and PDT derived from PEG-MoO_x NPs achieved enhanced therapeutic efficacy under 1064 nm irradiation compared to PTT alone under 808 nm irradiation *in vivo*.

3.6. Histology analysis of the mice injected with PEG-MoO_x NPs

As reported in some literature studies, mild hyperthermia treatment can improve the partial oxygen pressure by enhancing the blood flow in tumors, consequently improving the PDT efficiency.[51–54] In our experiments, after combining PTT and PDT, *in situ* caspase-3 staining (Fig. 10d) was used on the tissue sections of tumors to study the ability of NIR laser mediated therapy to elicit the apoptosis of tumors. It was found that high degrees of tumor cell necrosis and apoptosis (dark brown nuclei) in the combination therapy group were observed. H&E staining of the PANC-1 tumor slices was also carried out for tumors collected immediately after laser irradiation (Fig. 10e). As expected, significant damage of the cancer cells was noticed in the group with PEG-MoO_x NPs + 1064 nm laser irradiation compared with the PEG-MoO_x NPs + 808 nm group, but not in the other groups. This synergistic effect of PTT and PDT on a single nanoplatform mediated by 1064 nm irradiation indicated that PEG-MoO_x NPs could serve as a safe and effective phototherapeutic candidate for cancer treatment.

4. Conclusions

In summary, plasmonic PEG-MoO_x NPs with diameters of 15–25 nm have been synthesized through a simple, green, one-pot hydrothermal process and presented remarkable photoabsorption in the NIR biological window from 700 to 1200 nm. The PEG-MoO_x NPs displayed good biocompatibility and time-dependent cellular uptake. The *in vivo* biodistribution investigation indicated that most of the PEG-MoO_x NPs can be

excreted and biodegraded from the liver and spleen of mice after 30 days post-injection. Importantly, the phototherapy effects of the PEG-MoO_x nanoagent were investigated under NIR-I (808 nm) and NIR-II (1064 nm) irradiation. We firstly found that, upon 1064 nm irradiation at a low laser power output (0.6 W cm^{-2}), PEG-MoO_x NPs can not only convert light into heat with a mild hyperthermia (43 °C) but also generate ROS, which causes a far better tumor therapy effect in mice owing to the synergistic PTT and PDT effect than only inducing PTT exposure to the 808 nm laser (0.75 W cm^{-2}). The PEG-MoO_x-mediated PTT and PDT effect under 1064 nm laser irradiation was also proven by the percentage of cell death *in vitro*. The PDT effect of the exposure of PEG-MoO_x NPs to 1064 nm irradiation was further evidenced by a high level of ROS at the cellular level, extracellular ROS detection and ROS quenching under mild hyperthermia. The combination of PTT and PDT in the NIR-II window using the intelligent PEG-MoO_x nanoplatform provided new insight into cancer therapy in nanomedicine.

Conflicts of interest

There are no conflicts to declare.

Acknowledgements

This work was supported by the National Basic Research Programs of China (no. 2016YFA0201603, 2015CB932104), the Beijing Natural Science Foundation (2162046), the National Natural Science Foundation of China (51772293, 51772292, 11621505, 31571015, and 21320102003), and the Innovation Program of the Chinese Academy of Sciences (QYZDJ-SSW-SLH022).

References

1 P. Parhi, C. Mohanty and S. K. Sahoo, *Drug Discovery Today*, 2012, **17**, 1044–1052.
2 L. Cheng, C. Wang, L. Feng, K. Yang and Z. Liu, *Chem. Rev.*, 2014, **114**, 10869–10939.
3 S. B. Zhang, W. S. Guo, J. Wei, C. Li, X. J. Liang and M. Z. Yin, *ACS Nano*, 2017, **11**, 3797–3805.
4 J. Hu, Y. a. Tang, A. H. Elmenoufy, H. Xu, Z. Cheng and X. Yang, *Small*, 2015, **11**, 5860–5887.
5 H. Kim, K. Chung, S. Lee, D. H. Kim and H. Lee, *Wiley Interdiscip. Rev.: Nanomed. Nanobiotechnol.*, 2016, **8**, 23–45.
6 X. D. Zhang, H. Wang, A. L. Antaris, L. Li, S. Diao, R. Ma, A. Nguyen, G. Hong, Z. Ma, J. Wang, S. Zhu, J. M. Castellano, T. Wyss-Coray, Y. Liang, J. Luo and H. Dai, *Adv. Mater.*, 2016, **28**, 6872–6879.
7 Y. T. Zhong, G. Tian, Z. Gu, Y. Yang, L. Gu, Y. Zhao, Y. Ma and J. Yao, *Adv. Mater.*, 2014, **26**, 2831–2837.
8 A. M. Smith, M. C. Mancini and S. Nie, *Nat. Nanotechnol.*, 2009, **4**, 710–711.
9 X. Ding, C. H. Liow, M. Zhang, R. Huang, C. Li, H. Shen, M. Y. Liu, Y. Zou, N. Gao, Z. J. Zhang, Y. G. Li, Q. B. Wang, S. Z. Li and J. Jiang, *J. Am. Chem. Soc.*, 2014, **136**, 15684–15693.
10 N. Frazier and H. Ghandehari, *Biotechnol. Bioeng.*, 2015, **112**, 1967–1983.
11 Z. C. Wu, W. P. Li, C. H. Luo, C. H. Su and C. S. Yeh, *Adv. Funct. Mater.*, 2015, **25**, 6527–6537.
12 J. Ge, Q. Jia, W. Liu, M. Lan, B. Zhou, L. Guo, H. Y. Zhou, H. Y. Zhang, Y. Wang, Y. Gu, X. M. Meng and P. F. Wang, *Adv. Healthcare Mater.*, 2016, **5**, 665–675.
13 E. N. Cerón, D. H. Ortgies, B. del Rosal, F. Ren, A. Benayas, F. Vetrone, D. L. Ma, F. Sanz-Rodríguez, J. G. Solé, D. Jaque and E. M. Rodríguez, *Adv. Mater.*, 2015, **27**, 4781–4787.
14 C. Guo, H. Yu, B. Feng, W. Gao, M. Yan, Z. Zhang, Y. P. Li and S. Q. Liu, *Biomaterials*, 2015, **52**, 407–416.
15 L. M. Maestro, P. Haro-Gonzalez, B. del Rosal, J. Ramiro, A. J. Caamano, E. Carrasco, A. Juarranz, F. Sanz-Rodríguez, J. G. Solé and D. Jaque, *Nanoscale*, 2013, **5**, 7882–7889.
16 E. C. Dreaden, A. M. Alkilany, X. Huang, C. J. Murphy and M. A. El-Sayed, *Chem. Soc. Rev.*, 2012, **41**, 2740–2779.
17 R. Vankayala, C. C. Lin, P. Kalluru, C. S. Chiang and K. C. Hwang, *Biomaterials*, 2014, **35**, 5527–5538.
18 L. Gao, R. Liu, F. Gao, Y. Wang, X. Jiang and X. Gao, *ACS Nano*, 2014, **8**, 7260–7271.
19 R. Vankayala, Y. K. Huang, P. Kalluru, C. S. Chiang and K. C. Hwang, *Small*, 2014, **10**, 1612–1622.
20 B. Wang, J. H. Wang, Q. Liu, H. Huang, M. Chen, K. Li, C. Z. Li, X. Yu and P. K. Chu, *Biomaterials*, 2014, **35**, 1954–1966.
21 W. A. Murray and W. L. Barnes, *Adv. Mater.*, 2007, **19**, 3771–3782.
22 B. C. Marin, S. W. Hsu, L. Chen, A. Lo, D. W. Zwissler, Z. Liu and A. R. Tao, *ACS Photonics*, 2016, **3**, 526–531.
23 J. A. Faucheaux, A. L. D. Stanton and P. K. Jain, *J. Phys. Chem. Lett.*, 2014, **5**, 976–985.
24 X. Liu, W. C. Law, M. Jeon, X. Wang, M. Liu, C. Kim, P. N. Prasad and M. T. Swihart, *Adv. Healthcare Mater.*, 2013, **2**, 952–957.
25 S. Wang, A. Riedinger, H. Li, C. Fu, H. Liu, L. Li, T. L. Liu, L. F. Tan, M. J. Barthel, G. Pugliese, F. D. Donato, M. S. D'Abbusco, X. W. Meng, L. Manna, H. Meng and T. Pellegrino, *ACS Nano*, 2015, **9**, 1788–1800.
26 P. Kalluru, R. Vankayala, C. S. Chiang and K. C. Hwang, *Angew. Chem., Int. Ed.*, 2013, **52**, 12332–12336.
27 Z. Liu, X. Liu, X. Ran, E. Ju, J. Ren and X. Qu, *Biomaterials*, 2015, **69**, 56–64.
28 G. Ku, M. Zhou, S. Song, Q. Huang, J. Hazle and C. Li, *ACS Nano*, 2012, **6**, 7489–7496.
29 B. Liu, X. Zhao, Y. Xiao and M. Cao, *J. Mater. Chem. A*, 2014, **2**, 3338–3343.
30 G. Song, J. Shen, F. Jiang, R. Hu, W. Li, L. An, R. J. Zou, Z. G. Chen, Z. Y. Qin and J. Q. Hu, *ACS Appl. Mater. Interfaces*, 2014, **6**, 3915–3922.
31 G. Song, J. Hao, C. Liang, T. Liu, M. Gao, L. Cheng, J. Q. Hu and Z. Liu, *Angew. Chem., Int. Ed.*, 2016, **55**, 2122–2126.

32 T. Bao, W. Yin, X. Zheng, X. Zhang, J. Yu, X. Dong, Y. Yong, F. P. Gao, L. Yan, Z. J. Gu and Y. L. Zhao, *Biomaterials*, 2016, **76**, 11–24.
33 T. Anh Tran, K. Krishnamoorthy, Y. W. Song, S. K. Cho and S. J. Kim, *ACS Appl. Mater. Interfaces*, 2014, **6**, 2980–2986.
34 X. Zhao, M. Cao, B. Liu, Y. Tian and C. Hu, *J. Mater. Chem.*, 2012, **22**, 13334–13340.
35 V. Bhosle, A. Tiwari and J. Narayan, *J. Appl. Phys.*, 2005, **97**, 083539.
36 M. Ainwar, C. A. Hogarth and C. R. Theocharis, *J. Mater. Sci.*, 1989, **24**, 2387–2390.
37 M. R. Smith and U. S. Ozkan, *J. Catal.*, 1993, **141**, 124–139.
38 X. Ye, J. Fei, B. T. Diroll, T. Paik and C. B. Murray, *J. Am. Chem. Soc.*, 2014, **136**, 11680–11686.
39 Q. Yu, E. M. Rodriguez, R. Naccache, P. Forgione, G. Lamoureux, F. Sanz-Rodriguez, D. Scheglmann and J. A. Capobianco, *Chem. Commun.*, 2014, **50**, 12150–12153.
40 Q. Huang, S. Hu, J. Zhuang and X. Wang, *Chem. – Eur. J.*, 2012, **18**, 15283–15287.
41 N. S. Abadeer and C. J. Murphy, *J. Phys. Chem. C*, 2016, **120**, 4691–4716.
42 T. Zhang, R. Lan, C.-F. Chan, G.-L. Law, W.-K. Wong and K.-L. Wong, *Proc. Natl. Acad. Sci. U. S. A.*, 2014, **111**, E5492–E5497.
43 G. Pasparakis, *Small*, 2013, **9**, 4130–4134.
44 C. Seidl, J. Ungelenk, E. Zittel, T. Bergfeldt, J. P. Sleeman, U. Schepers and C. Feldmann, *ACS Nano*, 2016, **10**, 3149–3157.
45 T. Labouret, J. F. Audibert, R. B. Pansu and B. Palpant, *Small*, 2015, **11**, 4475–4479.
46 G. Pasparakis, *Small*, 2013, **9**, 4130–4134.
47 Z. Fan, X. Dai, Y. Lu, E. Yu, N. Brahmbatt, N. Carter, C. Tchouwou, A. K. Singh, Y. Jones, H. Yu and P. C. Ray, *Mol. Pharm.*, 2014, **11**, 1109–1116.
48 K. Deng, Z. Hou, X. Deng, P. Yang, C. Li and J. Lin, *Adv. Funct. Mater.*, 2015, **25**, 7280–7290.
49 F. Zhao, H. Meng, L. Yan, B. Wang and Y. Zhao, *Sci. Bull.*, 2015, **60**, 3–20.
50 Y. S. Takano, B. V. Harmon and J. F. R. Kerr, *J. Pathol.*, 1991, **163**, 329–336.
51 X. Yan, H. Hu, J. Lin, A. J. Jin, G. Niu, S. Zhang, P. Huang, B. Z. Shen and X. Y. Chen, *Nanoscale*, 2015, **7**, 2520–2526.
52 H. Zheng, J. Z. Ou, M. S. Strano and R. B. Kaner, *Adv. Funct. Mater.*, 2011, **21**, 2175–2196.
53 S. W. Hsu, W. Bryks and A. R. Tao, *Chem. Mater.*, 2012, **24**, 3765–3771.
54 C. W. Song, H. Park and R. J. Griffin, *Radiat. Res.*, 2001, **155**, 515–528.